Article | Open Access

Energy Materials

Wang *et al. Energy Mater.* **2026**, *6*, 600108 **DOI:**10.20517/energymater.2026.134

Synergistic iron-oxygen coordination in spent lithium iron phosphate slag for nitrate electroreduction to ammonia

Tianyu Wang[1,2], Yu Qing[1], Deyou Liu[1], Meiying Wei[1], Keqin Dai[3], Hongjie Guo[2,*], Hongliang Li[1,*]

Keywords:
Electrocatalytic nitrate reduction, Spent $LiFePO_4$, earth-abundant materials, small molecule conversion

Citation: Wang, T.; Qing, Y.; Liu, D.; Wei, M.; Dai, K.; Guo, H.; Li, H. Synergistic iron-oxygen coordination in spent lithium iron phosphate slag for nitrate electroreduction to ammonia. *Energy Mater.* **2026**, *6*, 600108. https://dx.doi.org/10.20517/energymater.2026.134

Received: 23 May 2026
First Decision: 12 Jun 2026
Revised: 2 Jul 2026
Accepted: 29 Jul 2026
Published: 26 Aug 2026

Academic Editor:
Yuping Wu
Copy Editor:
Shu-Yuan Duan
Production Editor:
Shu-Yuan Duan

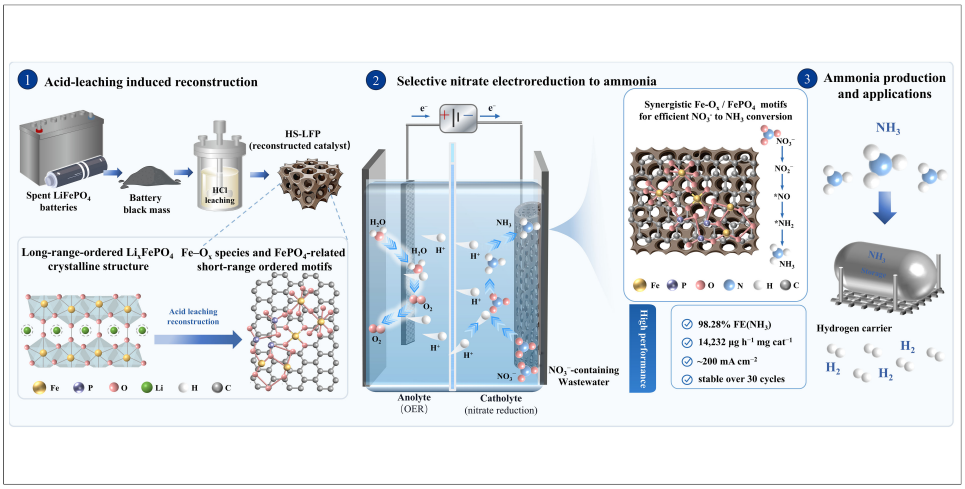

Abstract

The large-scale retirement of $LiFePO_4$ (LFP) batteries is generating increasing amounts of Fe- and P-rich lithium-extraction slag, which is discarded as low-value solid waste. Herein, we report the direct upcycling of spent LFP (S-LFP)-derived slag into a reconstructed Fe-based electrocatalyst for the nitrate reduction reaction (NO_3^-RR) to ammonia, which is widely recognized as a promising hydrogen carrier for future energy storage. Structural characterizations reveal that acid leaching deconstructs the olivine framework of S-LFP and reconstructs the slag into a disordered Fe-P-O matrix with a substantially enlarged specific surface area, featuring highly dispersed Fe-O_x species together with $FePO_4$-related short-range ordered motifs within a Fe-P-O framework. Electrochemical measurements show that, relative to commercial LFP and $FePO_4$, the reconstructed catalyst exhibits a more positive onset potential of ~ -0.05 V *vs.* reversible hydrogen electrode (RHE) and

[1]College of Mining Engineering, Taiyuan University of Technology, Taiyuan 030024, Shanxi, China.
[2]National Laboratory of Solid State Microstructures, School of Sustainable Energy and Resources, Jiangsu Key Laboratory of Artificial Functional Materials, Collaborative Innovation Center of Advanced Microstructures, Frontiers Science Center for Critical Earth Material Cycling, Nanjing University, Nanjing 215004, Jiangsu, China.
[3]School of International Education, Wuhan University of Technology, Wuhan 430070, Hubei, China.

***Correspondence to:** Dr. Hongjie Guo, National Laboratory of Solid State Microstructures, School of Sustainable Energy and Resources, Jiangsu Key Laboratory of Artificial Functional Materials, Collaborative Innovation Center of Advanced Microstructures, Frontiers Science Center for Critical Earth Material Cycling, Nanjing University, Nanjing 215004, Jiangsu, China. E-mail: 602025840006@smail.nju.edu.cn; Prof. Hongliang Li, College of Mining Engineering, Taiyuan University of Technology, Taiyuan 030024, Shanxi, China. lihongliang222@126.com

substantially enhanced NO_3^-RR activity. Combined *in situ* characterization and density functional theory calculations suggest that these coexisting Fe-O coordination motifs act cooperatively to regulate the local electronic structure, promote interfacial charge transfer, optimize the adsorption and conversion of nitrate-derived intermediates, and suppress the competing hydrogen evolution reaction. As a result, the waste-derived catalyst delivers a Faradaic efficiency of 98.28% and an NH_3 yield rate of 14,232 μg h^{-1} mg_{cat}^{-1} at -0.4 V *vs.* RHE. In addition, it shows stable performance over 30 consecutive cycles and can operate at current densities approaching 200 mA cm^{-2}. This work upcycles battery-recycling slags into Fe-P-O electrocatalysts via acid-leaching reconstruction for efficient NO_3^-RR toward sustainable ammonia and hydrogen-carrier applications.

INTRODUCTION

The rapid growth and large-scale retirement of $LiFePO_4$ (LFP) batteries have led to the continuous accumulation of spent cathode materials, posing increasing challenges for efficient recycling and sustainable waste management[1-4]. In current recycling processes, lithium (Li) recovery is typically prioritized, and acid leaching is widely adopted to extract Li from spent LFP (S-LFP) because of its operational simplicity and high extraction efficiency[5-7]. However, after Li extraction, large amounts of Fe- and P-rich leaching slag remain and are commonly treated as low-value solid waste[8-10]. Importantly, delithiation and acid-leaching do not merely remove Li; they also deconstruct the olivine framework, generate defects, and reconstruct the local coordination environment of the residual Fe-P-O matrix[11-13]. These structural and chemical evolutions indicate that S-LFP-derived slag is not only a recycling by-product, but also a promising precursor for the construction of functional materials and catalysts.

Electrocatalytic nitrate reduction has emerged as an attractive strategy for simultaneously addressing nitrate pollution and producing ammonia under ambient conditions[14-17]. Beyond its central role as a chemical feedstock, ammonia is widely regarded as a promising carbon-free hydrogen carrier because of its high hydrogen content and mature storage/transportation, and potential for on-demand hydrogen release. Therefore, electrochemical nitrate-to-ammonia conversion is particularly appealing not only for sustainable NH_3 synthesis but also for energy storage and hydrogen-carrier applications. This route is especially attractive because the industrial Haber-Bosch process relies on high temperature and high pressure, consumes substantial energy, and results in a large carbon footprint[18,19]. Compared with conventional thermal- or bio-assisted nitrate removal technologies, nitrate reduction reaction (NO_3^-RR) can be driven by renewable electricity under mild conditions and integrated into decentralized treatment systems, thereby offering a sustainable pathway for pollutant remediation and value-added chemical production[20-23]. Nevertheless, NO_3^-RR involves complex multi-step proton-coupled electron-transfer processes and multiple adsorbed intermediates, making catalytic activity and NH_3 selectivity highly dependent on the local coordination and electronic structure of active sites[24,25]. In this regard, Fe-based catalysts are particularly attractive because Fe centers can effectively mediate nitrate-derived intermediate conversion, while phosphate/oxygen coordination environments are expected to further tune the electronic structure, interfacial charge transfer, and stability of catalytic sites[26-29]. Therefore, converting S-LFP-derived Fe-P-O slag into NO_3^-RR electrocatalysts offers a compelling opportunity to couple battery-waste upcycling with nitrate valorization.

Building on this concept, recent studies have shown that top-down acid etching of S-LFP can break down the parent olivine framework and reconstruct the slag into Fe-based materials with unconventional local coordination environments, such as atomically dispersed O-coordinated Fe species and iron oxide/phosphate motifs[30]. This top-down reconstruction strategy not only preserves the intrinsic Fe/P coupling inherited from the parent phase, but also introduces abundant defects, increases surface exposure, and generates short-range ordered/disordered structures that are difficult to access through conventional

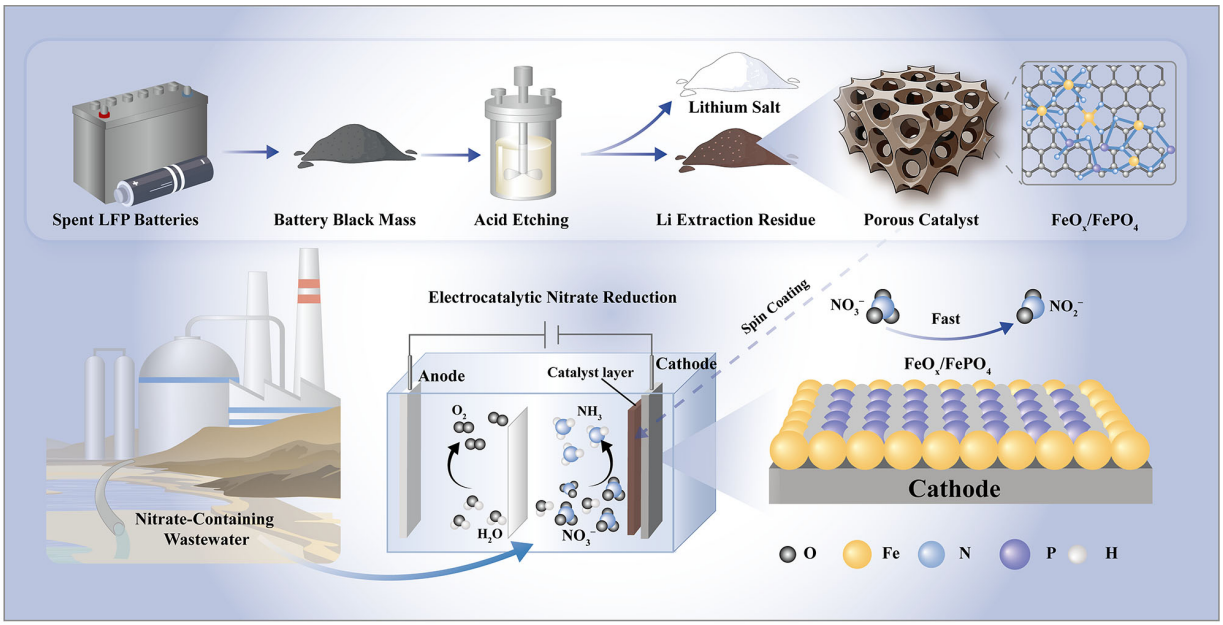

Figure 1. Schematic of the top-down reconstruction strategy for upcycling Spent $LiFePO_4$ (S-LFP) slags into electrocatalysts. Lithium extraction from S-LFP cathodes yields a solid slag that is conventionally discarded. Through acid-leaching-induced structural reconstruction, this low-value slag is transformed into a disordered Fe-P-O matrix (denoted HS-LFP) that serves as an efficient catalyst for electrocatalytic nitrate reduction to ammonia. The proposed local structural model of HS-LFP contains highly dispersed Fe-O_x species, neighboring Fe-O coordination motifs, and short-range ordered $FePO_4$-related domains within a reconstructed Fe-P-O matrix. LFP: $LiFePO_4$. HS-LFP: the S-LFP-derived slag.

bottom-up synthesis[31-34]. These advances suggest that acid-etched S-LFP-derived slags may serve as a unique structural platform for electrocatalysis. However, for NO_3^-RR, the reconstructed Fe-P-O framework may involve heterogeneous Fe-O/P coordination environments, potentially including Fe-O_x species and $FePO_4$-related short-range ordered motifs, yet their electronic coupling and catalytic effect remain poorly understood. Specifically, the synergistic effects of these coordination motifs on nitrate adsorption, interfacial charge transfer, intermediate conversion, and NH_3 selectivity are still poorly understood.

Herein, we report a top-down reconstruction strategy to directly upcycle S-LFP-derived slag into an efficient Fe-based electrocatalyst for NO_3^-RR to NH_3 [Figure 1]. Acid leaching deconstructs the parent olivine structure and reconstructs the slag into a disordered Fe-P-O framework, which, according to the combined characterization results, is consistent with highly dispersed Fe-O_x species and residual short-range ordered $FePO_4$-related domains. Combined structural characterization, electrochemical measurements, *in situ* Fourier transform infrared (FTIR) spectroscopy, and density functional theory (DFT) calculations reveal that these reconstructed Fe-O coordination motifs cooperatively modulate the local electronic environment, facilitate charge transfer, optimize nitrate-derived intermediate conversion, and suppress competing hydrogen evolution, thereby enabling selective NH_3 synthesis. In addition to wastewater treatment and value-added chemical production, the generated ammonia can serve as a hydrogen carrier, further highlighting the relevance of this waste-upcycling strategy to energy-material research. Overall, this work enables the sustainable high-value utilization of battery-recycling slag and provides insight into the coordination synergy of reconstructed Fe-based catalysts.

EXPERIMENTAL METHODS

Synthesis of HS-LFP catalyst

In this study, the S-LFP-derived slag (HS-LFP) catalyst was prepared by acid leaching [Supplementary Figure 1]. Initially, S-LFP battery black powder was selected as the starting material. The S-LFP cathode black

powder was obtained from discarded commercial LFP batteries provided by Changzhou Liyuan New Energy Technology Co., Ltd. Prior to processing, the spent batteries were fully discharged in 1 mol L^{-1} NaCl solution to a cut-off voltage of 0.5 V to eliminate residual electrical charge and ensure operational safety. After discharge, impurities were removed via mechanical dismantling and thermal treatment. The cathode was calcined at 350 °C for 2 h under an air atmosphere to remove residual organic binders and carbonaceous additives, and the LFP powder was scraped off the aluminum current collector. Subsequently, the collected powder was subjected to acid leaching in 2 mol L^{-1} HCl solution at room temperature for 10 min using a solid-liquid ratio of 0.1 g mL^{-1}, aiming to liberate lithium (Li) from the S-LFP framework. The Li recovery efficiency was quantified by ICP-OES based on the Li contents in the initial S-LFP powder and the acid-leached solid residue HS-LFP. The Li content decreased from 1.62 mmol g^{-1} in S-LFP to 0.08 mmol g^{-1} in HS-LFP, giving a Li recovery/removal efficiency of 95.06% according to [(1.62 - 0.08)/1.62] × 100%. The remaining precipitate was collected by filtration, repeatedly washed with deionized water and ethanol to remove residual acid and soluble impurities, and then dried at 60 °C for 4 h to obtain the Li-extracted slag, which is the HS-LFP employed in subsequent experiments.

Figure preparation

The schematic illustrations and graphical abstract were created by the authors using Photoshop, Adobe Illustrator, and Microsoft PowerPoint. Data plots were prepared using OriginPro. Structural models and DFT-related images were visualized using VESTA. Microscopy images were processed only for standard presentation purposes, such as cropping, scale-bar labeling, and brightness/contrast adjustment, using ImageJ. This information has been added to the manuscript as requested.

RESULTS AND DISCUSSION

Structural reconstruction and surface chemical features of HS-LFP catalyst

To clarify the structural evolution of the S-LFP-derived slag (HS-LFP) and identify the nature of its active centers, X-ray diffraction (XRD), transmission electron microscopy (TEM), scanning electron microscopy (SEM), energy dispersive X-ray spectroscopy (EDS), high-angle annular dark-field imaging (HAADF), and X-ray photoelectron spectroscopy (XPS) characterizations were conducted and systematically compared with S-LFP and commercial LFP and $FePO_4$ (FP).

As shown in Figure 2A, both LFP and S-LFP exhibit the characteristic diffraction features of olivine structure. The diffraction peak positions of S-LFP remain consistent with the standard pattern, while the attenuated peak intensity compared with that of LFP indicates partial loss of crystallinity after cycling. FP displays sharp and well-defined diffraction peaks, characteristic of a highly crystalline phase with long-range structural order. In contrast, HS-LFP shows no obvious diffraction features assignable to either $LiFePO_4$ or highly crystalline $FePO_4$, but only weak and broadened reflections, indicating substantial disruption of the long-range order of the parent lattice during acid leaching. A broad peak at around 26°, assigned to the graphite (002) plane, is also observed, originating from the carbon matrix. SEM [Supplementary Figure 2] reveals distinct morphological differences. LFP shows uniform spherical particles, while pure FP exhibits dense irregular bulks. In contrast, HS-LFP displays broken, rough-surfaced fragments, confirming acid-leaching-induced structural reconstruction rather than simple delithiation to S-LFP.

TEM images further show that S-LFP and HS-LFP exhibit significant differences in their microstructures. S-LFP primarily consists of relatively large flake- or lump-like particles with distinct boundaries, and its overall structure is relatively dense [Supplementary Figure 3]; high-resolution TEM images [Supplementary Figure 4] still reveal locally ordered regions. Fast Fourier transform (FFT) analysis of the selected area [Supplementary Figure 5A] gives an interplanar spacing of approximately 0.29 nm, which can be assigned to the (121) plane of an $LiFePO_4$-related structure, indicating that the material retains a relatively intact crystal

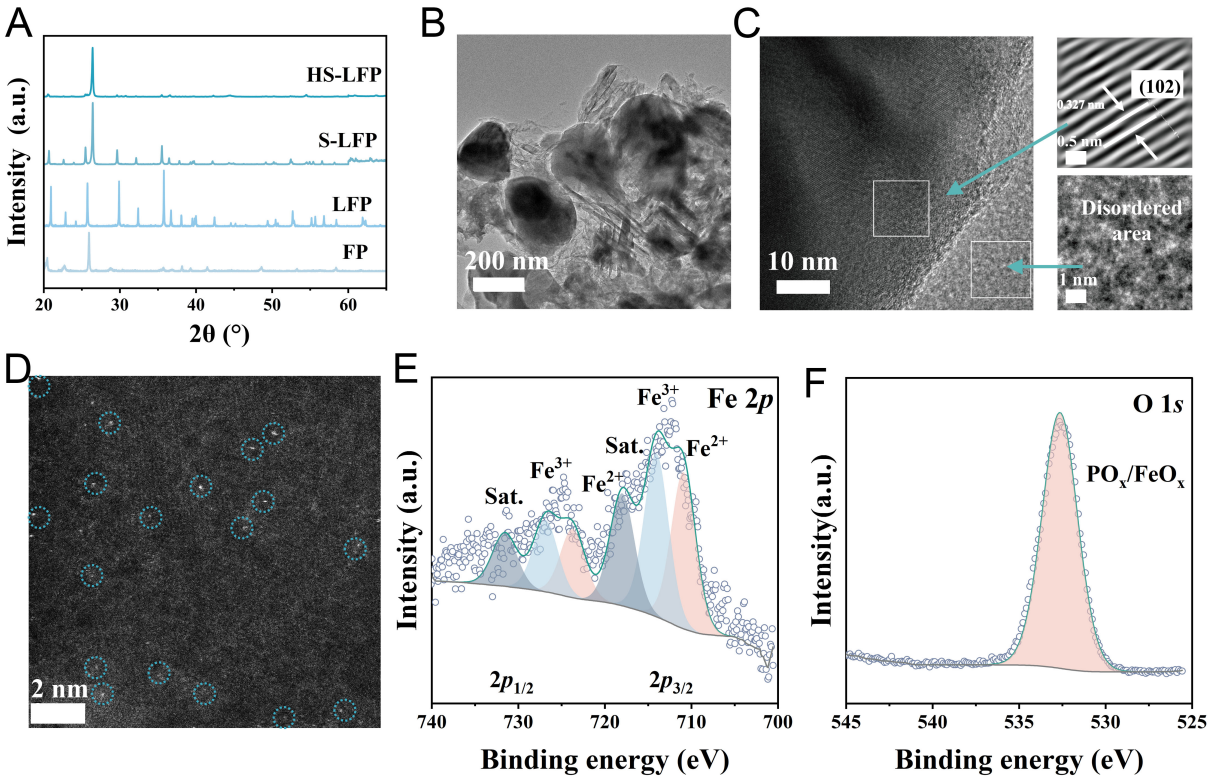

Figure 2. Structural and surface chemical characterization of the HS-LFP (A) XRD patterns of the HS-LFP, S-LFP, LFP and FP, together with the corresponding PDF references; (B) TEM image of the HS-LFP catalyst; (C) HRTEM image of the HS-LFP catalyst and enlarged lattice-fringe image from the selected region, showing an interplanar spacing of 0.327 nm corresponding to the (102) plane of a $FePO_4$-related structure and the disordered region; (D) HAADF-STEM image of the HS-LFP catalyst, the blue dashed circle highlights representative isolated bright contrast features assigned to highly dispersed Fe-related sites; (E) High-resolution Fe 2p XPS spectrum; (F) High-resolution O 1s XPS spectrum. S-LFP: Spent $LiFePO_4$; LFP: $LiFePO_4$; XRD: X-ray diffraction; FP: $FePO_4$; TEM: transmission electron microscopy; HRTEM: high-resolution transmission electron microscopy; HAADF-STEM: high-angle annular dark-field scanning transmission electron microscopy; XPS: X-ray photoelectron spectroscopy.

framework even after service. In contrast, HS-LFP exhibits an irregular, agglomerated, loose flake-like/flocculent structure with blurred particle edges [Figure 2B], accompanied by distinct fracturing features, reflecting the significant disruption of the original particle structure caused by the acid leaching process. In its HRTEM images [Figure 2C], most regions lack continuous lattice striations, with only a few short-range ordered regions remaining. FFT analysis [Supplementary Figure 5B] of the enlarged local region gives an interplanar spacing of approximately 0.327 nm, which can be assigned to the (102) plane of a $FePO_4$-related structure, indicating that minor local $FePO_4$ structural motifs are retained despite the destruction of long-range crystallinity. Meanwhile, another local region exhibits no discernible lattice fringes and is characteristic of a disordered domain. Combined with the XRD results, these observations confirm that the HS-LFP catalyst is not a uniform crystalline material, but a reconstructed system consisting of a disordered matrix and short-range ordered $FePO_4$ structural units.

The dispersion state of Fe sites was further examined by HAADF-STEM [Figure 2D]. No obvious Fe-based nanoparticles or clusters were detected; instead, uniformly dispersed isolated bright dots were observed on the reconstructed matrix. Given the Z-contrast mechanism of HAADF imaging, these observations suggest the presence of atomically dispersed Fe species. Elemental mapping [Supplementary Figure 6] further confirms that Fe atoms are homogeneously dispersed and closely co-localized with O species, supporting the presence of highly dispersed Fe species coordinated with surrounding oxygen species, without observable Fe aggregation at the nanoscale. Collectively, these results suggest that acid-leaching-induced reconstruction

stabilizes highly dispersed Fe-O_x species on the carbon-containing framework rather than inducing particle aggregation. XPS further reveals the chemical environment of the Fe centers [Figure 2E and F and Supplementary Figures 7 and 8]. Relative to S-LFP, HS-LFP exhibits a weakened Li 1s signal, indicating partial surface delithiation after acid leaching. The Fe 2p spectrum evolves from predominantly Fe^{2+} in S-LFP to a Fe^{3+}-enriched state in HS-LFP, together with residual Fe^{2+} and satellite features, evidencing delithiation-induced oxidation and electronic reconstruction of Fe sites. Meanwhile, the retained phosphate-region P 2p signal and the dominant PO_x/FeO_x component in O 1s indicate that Fe remains anchored in an oxygen-coordinated phosphate matrix. The coexistence of Fe^{2+}/Fe^{3+} species suggests multiple local Fe-O coordination environments, and the Fe^{3+}-enriched state of HS-LFP suggests substantial reconstruction of the local Fe-O coordination environment, possibly involving under-coordinated Fe species. Combined with the HRTEM and HAADF-STEM results, these data indicate that the Fe centers are stably anchored in oxygen-coordinated phosphate frameworks featuring coexisting short-range order and disorder regions. These observations are consistent with highly dispersed Fe-O_x species embedded in a heterogeneous Fe-P-O coordination environment, rather than a single uniform Fe coordination state.

In addition, EDS elemental mapping provides further evidence for the spatial distribution of elements. Compared with S-LFP [Supplementary Figures 9 and 10], the HS-LFP [Supplementary Figures 11-13] exhibits Fe, P, and Al loss and homogeneous distributions of Fe throughout the selected region, indicating good compositional uniformity of the framework. In particular, the Fe signal does not show localized aggregation, in agreement with the atomically dispersed Fe identified by HAADF-STEM. Elemental analysis of C and F further reveals an increased carbon content in HS-LFP (rising from 4.636% to 11.051%), which corroborates the retention of the carbon framework [Supplementary Figure 14].

Taken together, acid-leaching-induced Li extraction transforms S-LFP from its original long-range ordered olivine framework into a reconstructed structure composed of a disordered matrix with residual short-range ordered $FePO_4$-related units and highly dispersed Fe-O_x species. This architecture is fundamentally different from the regular bulk coordination environment in both S-LFP and LFP. The coexistence of structural disorder, short-range $FePO_4$-related domains, and highly dispersed Fe-O_x species is expected to increase the accessibility of Fe electrocatalytic centers and to reconstruct the local Fe-O-P coordination environment.

The exceptional electrocatalytic performance of the HS-LFP electrode in NO_3^-RR

Prior to evaluating the NO_3^-RR performance, the textural properties of HS-LFP were examined. The Li-extracted slag exhibits a dramatically enlarged specific surface area and porous structure. According to the N_2 adsorption-desorption results [Supplementary Figure 15], the specific surface area of HS-LFP reaches 139.00 $m^2 g^{-1}$, markedly higher than those of S-LFP (44.80 $m^2 g^{-1}$), FP (0.58 $m^2 g^{-1}$), and LFP (9.39 $m^2 g^{-1}$). This order-of-magnitude increase indicates that acid-leaching-induced reconstruction markedly increases the accessible surface area and interfacial exposure of the reconstructed Fe-P-O framework. Combined with the structural characterization, this enlarged surface is expected to expose more catalytically accessible Fe-O_x sites, thereby providing an important structural basis for enhanced reactant adsorption, electron transfer, and interfacial reaction kinetics during NO_3^-RR.

To evaluate the intrinsic electrocatalytic activity of different iron phosphate-based materials toward nitrate reduction, linear sweep voltammetry (LSV) measurements were first carried out in 1 M KOH and 1 M KOH + 0.1 M KNO_3 [Figure 3A]. All three electrodes display enhanced cathodic responses after the introduction of NO_3^-, indicating the participation of nitrate species in the cathodic reduction process. Notably, compared with FP and LFP, the HS-LFP electrode exhibits a more positive onset potential [-0.05 V *vs.* reversible hydrogen electrode (RHE)] and delivers consistently higher reduction current densities over the entire potential range, with a more pronounced current enhancement in the nitrate-containing electrolyte. This

result clearly suggests a stronger intrinsic catalytic activity of HS-LFP toward electrochemical NO_3^- reduction. To further clarify the kinetic origin of the outstanding catalytic behavior, electrochemical impedance spectroscopy (EIS) measurements were carried out. As shown in Figure 3B, the Nyquist plots reveal distinct differences in charge-transfer properties among the electrodes. Compared with FP and LFP, the HS-LFP electrode displays a smaller semicircle diameter, indicative of a lower charge-transfer resistance (R_{ct}) and faster interfacial electron transfer. A smaller R_{ct} means that the electron-coupled conversion of NO_3^- and its intermediates proceeds more readily on the electrode surface, which is particularly beneficial for the overall kinetics of this multi-electron reduction reaction. The electrochemically active surface area (ECSA) was estimated from the double-layer capacitance derived from cyclic voltammetry (CV) measurements [Figure 3C and Supplementary Figure 16]. The HS-LFP electrode exhibits the largest increase in capacitive current density with increasing scan rate, corresponding to the highest electrochemical double-layer capacitance (C_{dl}), which indicates a larger ECSA and thus more exposed real catalytic sites. This result is in excellent agreement with the specific surface area measurements, suggesting that the active sites generated after Li extraction not only provide a much larger physical surface area but also translate electrochemically into more accessible and operative interfacial active regions. Taken together, the LSV, EIS, and C_{dl} results suggest that the superior NO_3^-RR performance of HS-LFP arises from the reconstructed Fe-O/P coordination environments, the increased exposure of electrochemically accessible Fe-O_x sites within the heterogeneous Fe-P-O framework, and improved interfacial charge transfer.

As shown in Figure 3D, during continuous electrolysis from -0.2 to -0.6 V *vs.* RHE, the current density at each potential remains generally stable with time after a short initial transient decay. This initial decrease is commonly associated with double-layer rearrangement, gradual establishment of surface adsorbates, and stabilization of the local mass-transfer environment; the step-like fluctuations observed at -0.6 V *vs.* RHE are likely associated with bubble nucleation/detachment under high cathodic current density. In particular, near -0.4 V *vs.* RHE, the current response remains stable, and the current density reaches ~ 200 mA cm^{-2}, which is close to industrial scale, indicating that the HS-LFP electrode can sustain a relatively stable interfacial reaction state and continuous electron transfer process under NO_3^-RR. The step-like fluctuations in the -0.6 V curve arise from periodic H_2 bubble formation and detachment on the electrode surface under high cathodic potential, which temporarily alters the active area and local mass transport. This stable electrochemical behavior provides kinetic support for its simultaneously high Faradaic Efficiency (FE) and NH_3 yield. Prior to product quantification, the concentrations of NO_3^-, NO_2^-, and NH_4^+ were calibrated by ultraviolet-visible spectroscopy (UV-Vis) spectrophotometry using the corresponding standard curves [Supplementary Figure 17]. The high linear correlation coefficients ($R^2 \geq 0.998$) confirm the reliability of the detection method for subsequent performance calculations. Selectivity and ammonia production capability of the three electrodes were then quantitatively compared through product analysis. The HS-LFP electrode exhibits a superior FE(NH_3) over the most investigated potential range relative to the reference electrodes [Figure 3E]. In particular, at -0.4 V *vs.* RHE, the FE(NH_3) of HS-LFP reaches 98.28%, which is significantly higher than those of LFP and FP at the same potential. This result indicates that HS-LFP substantially suppresses the competing hydrogen evolution reaction (HER) under these conditions and directs electrons preferentially toward the NH_3 formation pathway. It is worth noting that further negative shifting of the potential to -0.5 and -0.6 V leads to a decrease in FE(NH_3) of HS-LFP (from 80.8% to 62.0%). This trend generally suggests that at higher overpotentials, interfacial HER begins to compete more strongly for active sites and electron supply, thereby compromising ammonia selectivity. In contrast, although LFP/FP also exhibit a certain degree of NH_3 selectivity at some potentials, their overall FE values remain clearly lower than that of HS-LFP. Consistent with the potential-dependent FE trend, the NH_3 yield results shown in Figure 3F further verify the performance advantage of HS-LFP. As the applied potential shifts from -0.2 to -0.6 V *vs.* RHE, the NH_3 yield of all three electrodes gradually increases, indicating that a more negative potential is beneficial for enhancing the overall reduction rate of NO_3^-RR. Importantly, the HS-LFP electrode

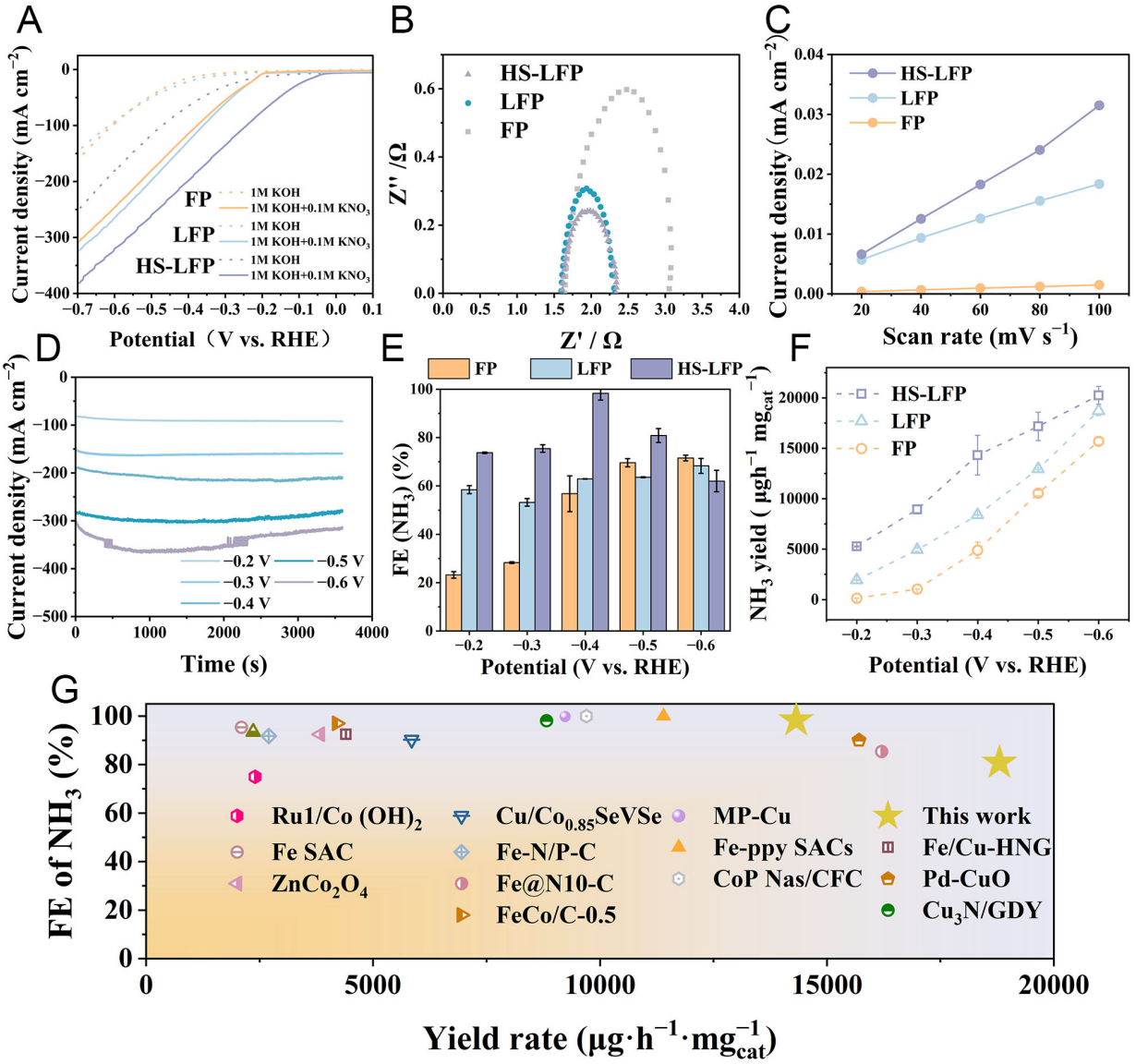

Figure 3. The exceptional electrochemical catalytic activity of the HS-LFP electrode toward nitrate reduction. (A) LSV curves of HS-LFP, LFP, and FP electrodes recorded in 1 M KOH and 1 M KOH + 0.1 M KNO_3; (B) Nyquist plots of HS-LFP, LFP, and FP electrodes; (C) Determination of double-layer capacitance from plots of capacitive current density versus scan rate; (D) Chronoamperometric curves of the HS-LFP electrode at different potentials in 1 M KOH + 0.1 M KNO_3; (E) Faradaic efficiency for NH_3 production on HS-LFP, LFP, FP electrodes at different applied potentials; (F) NH_3 yield rates of different electrodes as a function of applied potential; (G) Performance comparison with representative nitrate-to-ammonia electrocatalysts reported in the literature[35-48]. Error bars represent the standard deviation of three independent measurements (n = 3). FP: $FePO_4$; LFP: $LiFePO_4$; FE: Faradaic Efficiency; LSV: linear sweep voltammetry.

maintains the highest NH_3 production rate throughout the entire potential window and achieves an ammonia yield of 14,232 μg h^{-1} mg_{cat}^{-1} at -0.4 V *vs.* RHE, together with an FE(NH_3) of 98.28%, demonstrating the optimal balance between activity and selectivity. Although the NH_3 yield can still increase at more negative potentials, the accompanying decline in FE indicates that the system gradually departs from the optimal selectivity window. Therefore, -0.4 V *vs.* RHE can be identified as the optimal operating potential for efficient NO_3^--to-NH_3 conversion on the HS-LFP electrode.

Finally, the NO_3^--to-NH_3 performance of the HS-LFP electrode was compared with representative catalysts reported in the literature [Supplementary Table 1 and Figure 3G]. The results show that HS-LFP can achieve a $FENH_3$ as high as 98.28% and an ammonia yield of 14,232 μg h^{-1} mg_{cat}^{-1} in a mild alkaline electrolyte, which

compares favorably with many representative catalysts reported under comparable conditions. The ability to selectively generate NH_3 at a high rate is particularly meaningful because ammonia can function as a hydrogen carrier for future carbon-free energy systems. Considering that HS-LFP is derived from the Li-extraction slag generated during S-LFP recycling, this result not only demonstrates that the discarded iron phosphate fraction can be transformed from a low-value solid waste into a high-value electrocatalyst, but also highlights that Li-deficient reconstruction and interfacial engineering can effectively unlock the catalytic potential of $Fe\text{-}O_4$/$Fe\text{-}O_6$/$FePO_4$ sites in waste slags for NO_3^- reduction.

Mechanistic insights into nitrate electroreduction on HS-LFP

To clarify the origin of NH_3 formation and the intrinsic catalytic mechanism of HS-LFP toward nitrate electroreduction, a series of isotope-labeling, *in situ* spectroscopic, and theoretical analyses were carried out. As shown in Supplementary Figure 18, negligible NH_3 was produced when using a blank carbon paper (CP) electrode in the presence of NO_3^- or when using the HS-LFP catalyst in a nitrate-free electrolyte. The high ammonia yield was only achieved when both the HS-LFP catalyst and NO_3^- ions were present, ruling out the possibility of nitrogen contamination from the environment or catalyst decomposition. This was further corroborated by ^{15}N isotope labeling experiments [Figure 4A]. The hydrogen-1 nuclear magnetic resonance (^1H NMR) spectrum of the electrolyte after electrolysis with $^{15}NO_3^-$ as the nitrogen source exhibited a distinct doublet characteristic of $^{15}NH_4^+$, while a triplet was observed when $^{14}NO_3^-$ was used. The isotope-tracing observations confirm that the synthesized ammonia originates exclusively from the electroreduction of NO_3^-. The regulation of hydrogen-related intermediates is an important factor in achieving high FE for NO_3^-RR. We utilized electron paramagnetic resonance (EPR) spectroscopy with DMPO as a spin-trapping agent to monitor the behavior of reactive hydrogen species at the catalyst interface [Figure 4B]. In the nitrate-free electrolyte, a robust 1:2:2:1 quadruple signal characteristic of DMPO-H was observed, indicating the accumulation of DMPO-detectable hydrogen-related species on the electrode surface. Conversely, upon the introduction of NO_3^-, the DMPO-H signal intensity drastically diminished. This decrease indicates that DMPO-detectable hydrogen-related species no longer accumulate to a measurable level under NO3¯RR conditions. However, this signal decrease should not be interpreted solely as direct evidence of H* consumption, because competitive adsorption or site blocking by NO_3^-/nitrate-derived intermediates may also suppress the steady-state generation or accumulation of hydrogen-related species. Therefore, the EPR results suggest that, in the presence of NO_3^-, hydrogen-related intermediates are preferentially involved in nitrate hydrogenation and/or prevented from accumulating because of nitrate-related surface adsorption processes, thereby contributing to the high NH_3 selectivity.

The evolution of adsorbed intermediates was monitored by *in situ* FTIR spectroscopy under different applied potentials [Figure 4C]. As cathodic polarization increases, the spectral features of nitrate-derived species evolve continuously, indicating a potential-dependent transformation of surface adsorbates/intermediates during the NO_3^-RR process. Based on prior *in situ* FTIR studies, the bands observed at around 1,090, 1,160, 1,236, 1,349 and 1,479 cm^{-1} can be tentatively associated with nitrate-reduction-related surface species, including N-O stretching / NH_2OH-related species, NO_2^--related vibrations, NO_3^--related vibrations and NH_4^+/NH_3 -related deformation modes. The broad feature near 1,638 cm^{-1} may also include a significant contribution from the bending vibration of interfacial H_2O. Therefore, some of these assignments should be regarded as tentative because overlap from interfacial water, hydroxyl species, electrolyte-derived species, and the phosphate-containing catalyst framework cannot be fully excluded. Nevertheless, the overall spectral evolution supports a stepwise nitrate-to-ammonia conversion pathway involving multiple oxygenated and hydrogenated nitrogen intermediates[49-52].

To elucidate the structural origin of the exceptional catalytic performance of HS-LFP, particularly the possible synergy among highly dispersed $Fe\text{-}O_x$ sites and neighboring $FePO_4$ motifs within the reconstructed framework, DFT calculations were performed using two representative structural models, namely, a $FePO_4$

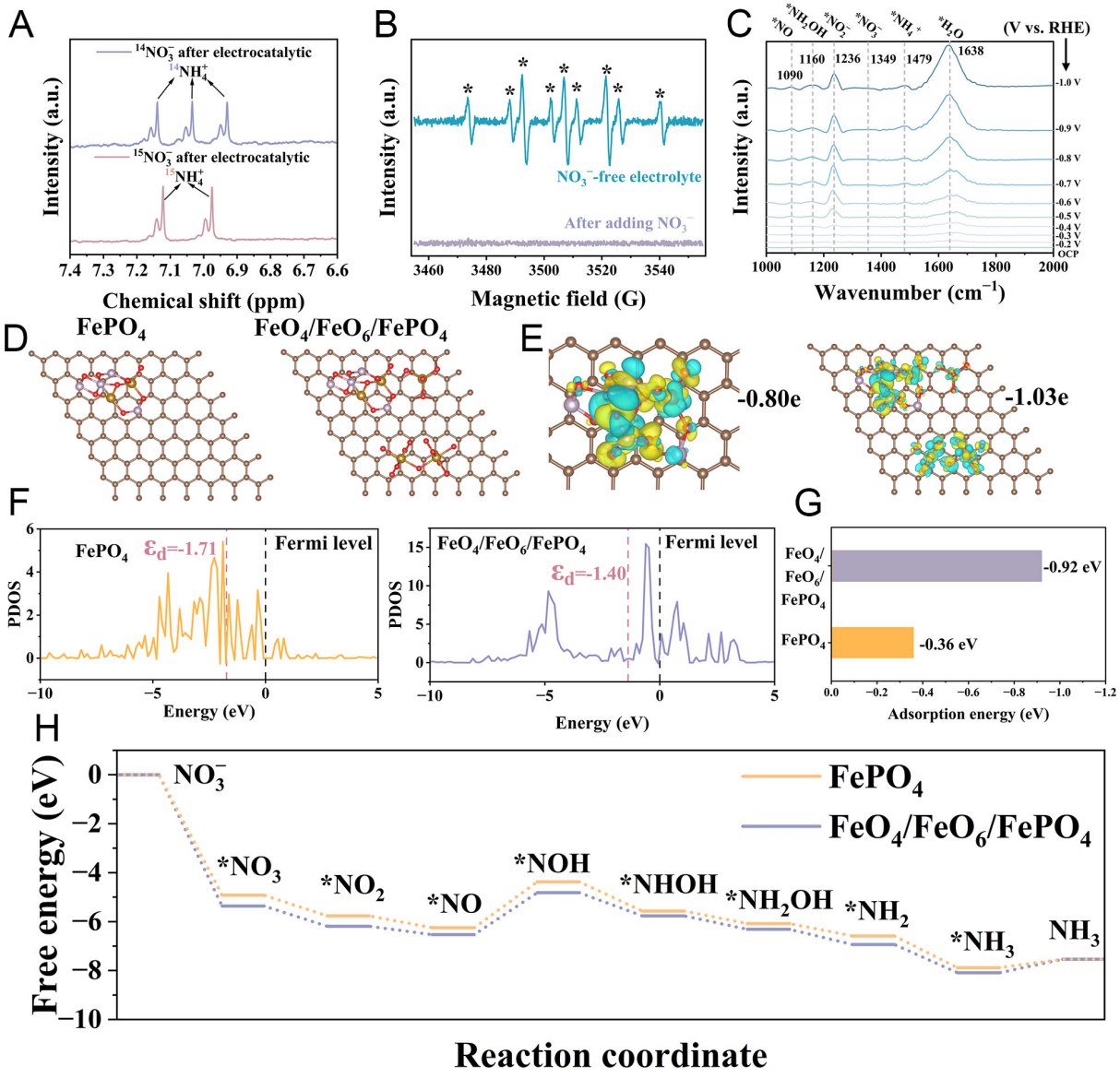

Figure 4. Mechanistic investigation of nitrate electroreduction on HS-LFP. (A) ^{1}H NMR spectra of products after electrolysis in $^{14}NO_3^-$ and $^{15}NO_3^-$-containing electrolytes; (B) EPR spectra recorded in nitrate-free electrolyte and after NO_3^- addition. * indicates the characteristic peaks of the DMPO-H adduct; (C) *In-situ* FTIR spectra collected at different applied potentials; (D) Atomic structure models of $FePO_4$ and Fe-O_4/Fe-O_6/$FePO_4$; (E) Charge density difference diagrams for reactant adsorption on the two catalysts, with net electron transfer labeled; (F) PDOS of Fe d-orbitals in $FePO_4$ and Fe-O_4/Fe-O_6/$FePO_4$, with d-band center and Fermi level indicated; (G) Comparison of NO_3^- adsorption energies on the two catalysts; (H) Free energy diagrams for nitrate reduction to NH_3 on $FePO_4$ and Fe-O_4/Fe-O_6/$FePO_4$ representative models respectively. RHE: Reversible hydrogen electrode; PDOS: projected density of states; ^{1}H NMR: hydrogen-1 nuclear magnetic resonance; HS-LFP: the S-LFP-derived slag; EPR: electron paramagnetic resonance; FTIR: Fourier transform infrared.

model and a heterogeneous $FeO_4/FeO_6/FePO_4$ model. The latter is not intended to represent the exact structure of HS-LFP, but rather an experimentally constrained local coordination model. This choice is based on the combined characterization results: XRD and HRTEM indicate that HS-LFP mainly consists of a disordered matrix with residual short-range ordered $FePO_4$ domains, while HAADF-STEM and XPS suggest highly dispersed Fe species embedded in heterogeneous Fe-O/P coordination environments with multiple Fe valence/coordinative states. Therefore, the $FePO_4$ unit was used to represent the retained short-range ordered phosphate-related motif, and the FeO_4 and FeO_6 units were introduced to mimic the coexistence of

low-coordinated and relatively saturated Fe-O sites in the reconstructed matrix. This model was thus designed to capture the essential local coordination heterogeneity and the possible electronic synergy among adjacent Fe-O motifs in HS-LFP [Figure 4D]. It should also be noted that the graphene support used in the calculation is an idealized conductive carbon model rather than an exact representation of the carbon phase in the real electrode. The experimental carbon environment contains both disordered carbon components and relatively more graphitized carbon paper. Therefore, the calculations are mainly used to reveal qualitative electronic-structure trends of the Fe-O-P active motif at a conductive interface, while possible quantitative effects from the real non-ideal carbon support cannot be fully excluded. The charge-density-difference results further support the above conclusion. As shown in Figure 4E, the yellow and blue colors represent electron accumulation and electron depletion, respectively. Upon adsorption, pronounced charge redistribution is observed around the Fe-O_4 sites and their adjacent coordination environment, indicating strong interfacial electronic coupling between the adsorbate and catalyst surface. Notably, the Fe-O_4/Fe-O_6/$FePO_4$ model exhibits a larger magnitude of charge transfer upon adsorption (-1.03 e^-) than the reference model (-0.80 e^-), suggesting a more substantial electron reorganization induced by adsorption. This result suggests that neighboring Fe-O_6 sites can modulate the local electronic environment of low-coordination Fe sites through a cooperative effect. Such localized charge polarization is expected to facilitate the activation of nitrate-derived species and optimize the adsorption strength of key intermediates, thereby promoting the overall reaction kinetics. This electronic modulation is also reflected in the projected density of states (PDOS) results [Figure 4F]. For the $FePO_4$ model, the d-band center is located at -1.71 eV, whereas for the FeO_4/FeO_6/$FePO_4$ model, it shifts upward to -1.40 eV, closer to the Fermi level (E_F = 0 eV). The upshift of the d-band center indicates that the reconstructed coordination-synergistic structure endows the Fe-O_4 site with a more suitable electronic configuration for interacting with nitrate-derived intermediates, thereby enhancing intermediate adsorption and activation and facilitating subsequent conversion steps. The adsorption-energy comparison shown in Figure 4G provides additional evidence for this synergistic effect. The FeO_4/FeO_6/$FePO_4$ model exhibits a more favorable adsorption energy of -0.92 eV, significantly lower than that of the $FePO_4$ model (-0.36 eV), indicating stronger interaction with nitrate-related species. This result suggests that the Fe-O_4-centered synergistic configuration is more capable of capturing and activating nitrate at the initial stage of the reaction. The calculated free-energy profiles further reveal the origin of the improved catalytic performance [Figure 4H]. Both models follow a multistep pathway involving *NO_3, *NO_2, *NO, *NOH, *NHOH, *NH_2OH, *NH_2, and *NH_3 intermediates before the final NH_3 release [Supplementary Figures 19 and 20]. Notably, the FeO_4/FeO_6/$FePO_4$ model consistently exhibits a lower free-energy profile than the $FePO_4$ model, especially for the uphill hydrogenation step associated with the formation of *NOH. This step is identified as the rate-determining step, and the corresponding energy barrier decreases from 1.8802 eV on $FePO_4$ to 1.718 eV on the Fe-O_4-centered synergistic model.

Overall, the mechanistic results collectively demonstrate that the excellent NO_3^-RR performance of HS-LFP is attributed to reconstructed Fe-O_x active sites within a heterogeneous Fe-P-O coordination environment, together with electronic synergy from adjacent coordination motifs. In the model, the Fe-O_4 site acts as the primary catalytic center for nitrate adsorption and conversion, while the surrounding Fe-O_6/$FePO_4$ environment tunes its charge distribution, shifts the d-band center toward the Fermi level, strengthens nitrate adsorption, and reduces the rate-determining barrier from 1.8802 to 1.718 eV. This coordination-synergistic mechanism provides a clear explanation for the enhanced activity and selectivity of HS-LFP toward ammonia electrosynthesis from nitrate.

Practical viability of HS-LFP for nitrate-to-ammonia electrosynthesis

Ammonia is an important value-added chemical and a promising hydrogen carrier. Therefore, the practical performance of HS-LFP for ammonia production requires further verification. Since HS-LFP possesses high intrinsic activity and favorable interfacial regulation for nitrate reduction, we further evaluated its

performance in terms of continuous-flow compatibility, cycling durability, stability, and techno-economic feasibility. As illustrated in Figure 5A, a flow-cell system was constructed to evaluate the application potential of HS-LFP for electrocatalytic nitrate-to-ammonia conversion. The corresponding current-density response over 30 successive cycles is provided in Supplementary Figure 21 (with the cycle number on the x-axis), showing that HS-LFP maintains a stable cathodic current throughout repeated operations. As shown in Supplementary Figures 22-24, the bright isolated contrast features assigned to atomically dispersed Fe species are still clearly observed after the cycle-stability test, and no obvious Fe aggregation, nanoparticle formation, or phase segregation is detected. Meanwhile, XRD and XPS analyses demonstrate that no obvious degradation occurs to the catalyst upon repeated stability testing, with the chemical environment of Fe largely preserved [Supplementary Figures 25-27]. Moreover, the catalyst does not lose its nitrate reduction capability at 100 ppm; rather, it still sustains a measurable and non-negligible NH_3 selectivity even when the nitrate concentration is reduced to the millimolar level [Supplementary Figure 28].

A photograph of the assembled flow-cell system is shown in Supplementary Figure 29. In this configuration, nitrate-containing wastewater is continuously supplied to the cathode compartment, where HS-LFP serves as the NO_3^-RR catalyst, while the anodic side drives the oxygen evolution reaction. This design highlights a direct utilization route of S-LFP-derived HS-LFP for continuous nitrate conversion.

The operational robustness of the HS-LFP catalytic system and its resistance to competitive ions were first assessed by a 30-cycle test in simulated wastewater containing 1 M KOH, 0.1 M KNO_3, 0.1 M KCl, and 0.1 M K_2SO_4 at a constant potential of -0.4 V *vs.* RHE. As shown in Figure 5B, both the FE(NH_3) and NH_3 yield remain highly stable over repeated cycling, with the FE maintained at around 95% and the ammonia yield rate remaining nearly unchanged throughout 30 consecutive runs. These results indicate that HS-LFP possesses good tolerance to representative coexisting anions such as chloride and sulfate under the tested conditions and can sustain stable nitrate reduction performance in complex electrolyte environments. To further assess its durability under continuous operation, HS-LFP was examined in the flow-cell mode over extended electrolysis.

As shown in Figure 5C, the FE(NH_3) remains at a high level during the initial stage of continuous operation and shows a moderate decline after prolonged electrolysis. This decline is likely related to the combined effects of bulk nitrate consumption, progressively enhanced interfacial mass-transport limitation, and local microenvironment variation during sustained operation, rather than solely reflecting intrinsic catalyst deactivation. As nitrate is continuously consumed, insufficient nitrate replenishment near the catalyst surface weakens the kinetic advantage of NO_3^- RR over HER, leading to a gradual decrease in NH_3 selectivity.

Beyond electrochemical performance, HS-LFP also exhibits low-cost preparation potential. As shown in Supplementary Figure 30 and Figure 5D, the estimated cost of HS-LFP is approximately 0.01 USD g^{-1} when considering direct preparation cost only. This value represents a theoretical lower-bound estimate rather than a full production cost, as it excludes battery collection, disassembly, waste neutralization, labor, and capital-related expenses. Therefore, the comparison with literature-reported Fe-N-C/metal-organic framework (MOF) and Fe-N-C/single-atom catalyst (SAC) catalysts should be interpreted with caution because of the different accounting boundaries. Even under more conservative assumptions that include waste neutralization and minimum manual handling (see Supplementary Materials), HS-LFP still retains a clear feedstock-cost advantage owing to the near-zero raw material cost of the S-LFP-derived slag. These results highlight the economic attractiveness of waste-derived HS-LFP as a catalyst platform for nitrate-to-ammonia electrosynthesis.

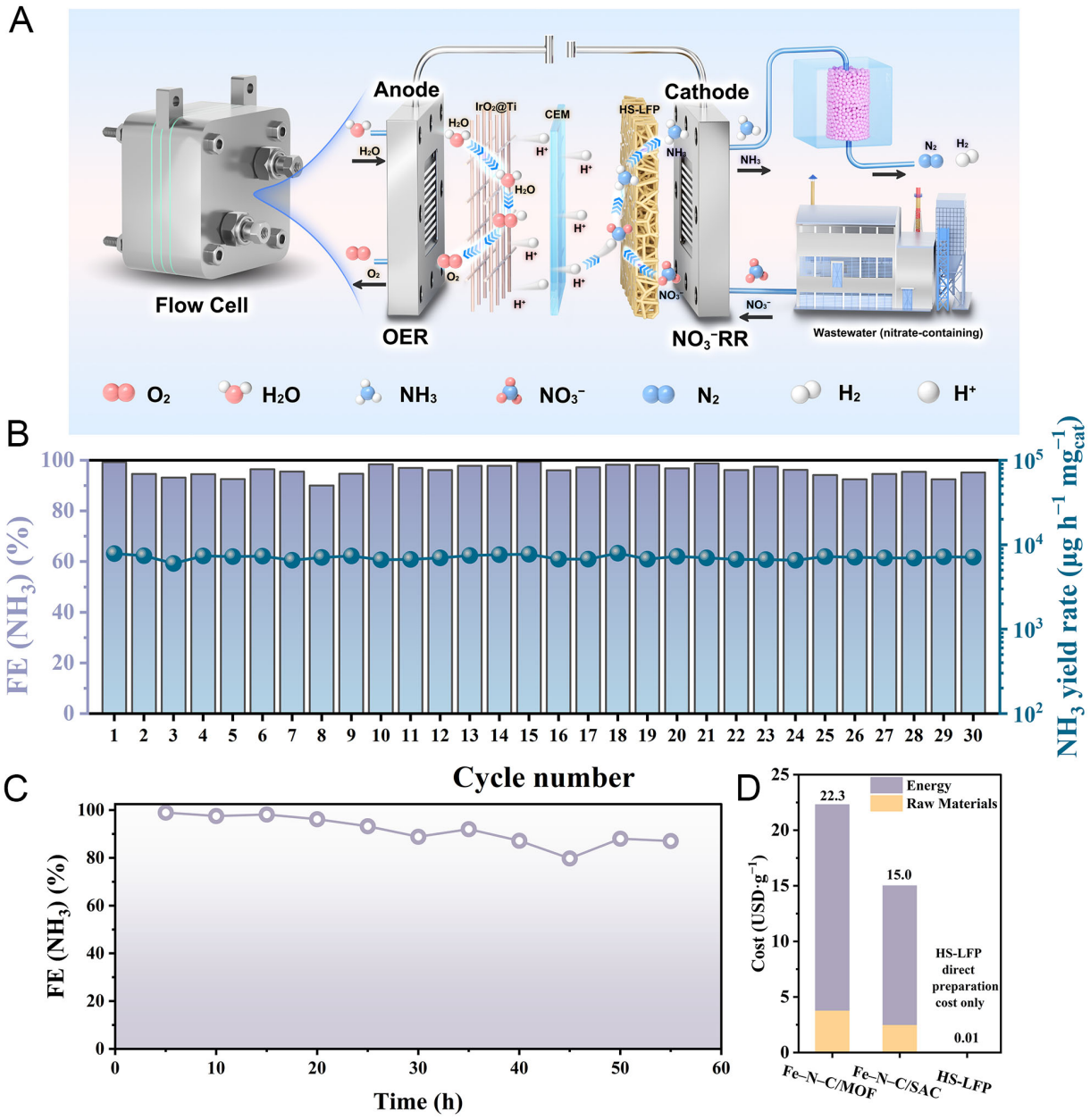

Figure 5. Practical applicability, durability evaluation, and cost analysis of HS-LFP for nitrate-to-ammonia electrosynthesis. (A) Schematic illustration of the flow-cell configuration for continuous electrocatalytic nitrate reduction, where HS-LFP serves as the cathodic catalyst for NO_3^-RR and IrO_2@Ti is used as the anodic OER electrode; (B) Cycling stability of HS-LFP over 30 consecutive runs in simulated wastewater containing 1 M KOH, 0.1 M KNO_3, 0.1 M KCl, and 0.1 M K_2SO_4 at -0.4 V *vs.* RHE, showing the NH_3 Faradaic efficiency and NH_3 yield rate; (C) Long-term NH_3 Faradaic efficiency of HS-LFP during continuous operation in the flow-cell system; (D) Simplified cost comparison under different accounting scopes, including HS-LFP (direct preparation cost only) and representative literature values for Fe-N-C/MOF and Fe-N-C/SAC catalysts. CEM: Cation exchange membrane; HS-LFP: the S-LFP-derived slag; OER: oxygen evolution reaction; NO_3^-RR: nitrate reduction reaction; FE: Faradaic Efficiency; SAC: single-atom catalyst; MOF: metal-organic framework; RHE: reversible hydrogen electrode.

CONCLUSION

We developed a sustainable strategy to upcycle S-LFP-derived Li-extraction slag into a reconstructed Fe-based electrocatalyst containing highly dispersed Fe-related species for efficient nitrate electroreduction to ammonia. Acid-leaching-induced reconstruction transforms the original olivine framework into a reconstructed Fe-P-O matrix containing multiple highly dispersed Fe-O_x species and residual short-range

ordered $FePO_4$-related motifs within a reconstructed Fe-P-O matrix. Mechanistic investigations and DFT calculations based on a representative local model suggest that Fe-O_4-like sites may serve as the primary catalytic centers, while neighboring Fe-O_6/$FePO_4$-related motifs provide synergistic electronic regulation that optimizes intermediate adsorption and lowers the reaction barrier. Consequently, the reconstructed catalyst achieves a $FENH_3$ of 98.28% and an NH_3 yield rate of 14,232 μg h^{-1} mg_{cat}^{-1} at -0.4 V *vs.* RHE, together with robust cycling stability and durable continuous-flow performance.

This work highlights a dual-benefit pathway that couples spent-battery upcycling with nitrate wastewater valorization, and demonstrates how coordination reconstruction within waste-derived frameworks can be leveraged to create efficient Fe-based electrocatalysts. Apart from wastewater remediation and ammonia production, the obtained ammonia acts as a hydrogen carrier and is essential for future sustainable energy systems.

DECLARATIONS

Authors' contributions

Methodology: Wang, T.
Investigation: Wang, T.; Qing, Y.; Liu, D.; Wei, M.; Dai, K.; Guo, H.
Validation: Wang, T.; Qing, Y.; Wei, M.
Visualization: Wang, T.; Dai, K.; Guo, H.
Writing - original draft: Wang, T.
Data curation: Qing, Y.; Liu, D.
Data presentation: Dai, K.
Supervision: Guo, H.; Li, H.
Conceptualization: Guo, H.
Writing - review & editing: Guo, H.; Li, H.
Supervision: Li, H.
Project administration: Li, H.
Funding acquisition: Li, H.

Availability of data and materials

The data supporting the findings of this study are available within this Article and its Supplementary Materials. Further data are available from the corresponding authors upon request.

AI and AI-assisted tools statement

Not applicable.

Financial support and sponsorship

This work was supported by the following funding sources: the 2025 Central Government Guidance for Local Science and Technology Development Fund Project (YDZJSX2025D092), the Fundamental Research Program of Shanxi Province (202203021221041), and the Anhui Engineering Research Center for Coal Clean Processing and Carbon Reduction (CCCE-2023002). The authors gratefully acknowledge this support.

Conflict of Interest

All authors declared that there are no conflicts of interest.

Ethical approval and consent to participate

Not applicable.

Consent for publication

Not applicable.

Copyright

Supplementary Materials

Supplementary Materials

REFERENCES

1. Gu, X.; Feng, X.; Yang, S.; et al. Photovoltaic-driven dual-oxidation seawater electrolyzer for sustainable lithium recovery. *Proc. Natl. Acad. Sci. U. S. A.* **2024**, *121*, e2414741121. DOI PubMed PMC
2. Zhao, J.; Zhou, F.; Wang, H.; et al. Co-recovery of spent $LiCoO_2$ and $LiFePO_4$ by paired electrolysis. *Green. Chem.* **2024**, *26*, 456-65. DOI
3. Zhang, Y.; Li, J.; Zhao, W.; et al. Complete metal recycling from lithium-ion batteries enabled by hydrogen evolution catalyst reconstruction. *J. Am. Chem. Soc.* **2023**, *145*, 27740-7. DOI
4. Kim, K.; Raymond, D.; Candeago, R.; Su, X. Selective cobalt and nickel electrodeposition for lithium-ion battery recycling through integrated electrolyte and interface control. *Nat. Commun.* **2021**, *12*, 6554. DOI PubMed PMC
5. Yu, J.; Wang, X.; Zhou, M.; Wang, Q. A redox targeting-based material recycling strategy for spent lithium ion batteries. *Energy. Environ. Sci.* **2019**, *12*, 2672-7. DOI
6. Tran, M. K.; Rodrigues, M. F.; Kato, K.; Babu, G.; Ajayan, P. M. Deep eutectic solvents for cathode recycling of Li-ion batteries. *Nat. Energy.* **2019**, *4*, 339-45. DOI
7. Fan, E.; Li, L.; Wang, Z.; et al. Sustainable recycling technology for Li-ion batteries and beyond: challenges and future prospects. *Chem. Rev.* **2020**, *120*, 7020-63. DOI
8. Baum, Z. J.; Bird, R. E.; Yu, X.; Ma, J. Lithium-ion battery recycling - overview of techniques and trends. *ACS. Energy. Lett.* **2022**, *7*, 712-9. DOI
9. Li, M.; Mo, R.; Ding, A.; Zhang, K.; Guo, F.; Xiao, C. Electrochemical technology to drive spent lithium-ion batteries (LIBs) recycling: recent progress, and prospects. *Energy. Mater.* **2024**, *4*, 400070. DOI
10. Arnold, S.; Ruthes, J. G. A.; Kim, C.; Presser, V. Electrochemical recycling of lithium-ion batteries: advancements and future directions. *EcoMat* **2024**, *6*, e12494. DOI
11. Yan, S.; Jiang, Y.; Chen, X.; et al. Engineering classification recycling of spent lithium-ion batteries through pretreatment: a comprehensive review from laboratory to scale-up application. *Rare. Metals.* **2024**, *43*, 915-41. DOI
12. Wu, J.; Xiao, L.; Shen, L.; et al. Recent advancements in hydrometallurgical recycling technologies of spent lithium-ion battery cathode materials. *Rare. Metals.* **2024**, *43*, 879-99. DOI
13. Guo, Y.; Yao, Y.; Guo, C.; et al. Atomistic observation and transient reordering of antisite Li/Fe defects toward sustainable $LiFePO_4$. *Energy. Environ. Sci.* **2024**, *17*, 7749-61. DOI
14. Xu, B.; Li, D.; Zhao, Q.; Feng, S.; Peng, X.; Chu, P. K. Electrochemical reduction of nitrate to ammonia using non-precious metal-based catalysts. *Coord. Chem. Rev.* **2024**, *502*, 215609. DOI
15. Xiong, Y.; Wang, Y.; Zhou, J.; Liu, F.; Hao, F.; Fan, Z. Electrochemical nitrate reduction: ammonia synthesis and the beyond. *Adv. Mater.* **2024**, *36*, e2304021. DOI
16. Huang, H.; Peramaiah, K.; Huang, K. Rethinking nitrate reduction: redirecting electrochemical efforts from ammonia to nitrogen for realistic environmental impacts. *Energy. Environ. Sci.* **2024**, *17*, 2682-5. DOI
17. Zhang, H.; Wang, H.; Cao, X.; et al. Unveiling cutting-edge developments in electrocatalytic nitrate-to-ammonia conversion. *Adv. Mater.* **2024**, *36*, e2312746. DOI
18. Zhong, W.; Gong, Z.; Chen, P.; et al. Electrochemical reduction of nitrate to ammonia: From fundamental understanding to practical applications. *Chem. Catalysis.* **2024**, *4*, 101060. DOI
19. Fan, J.; Arrazolo, L. K.; Du, J.; et al. Effects of ionic interferents on electrocatalytic nitrate reduction: mechanistic insight. *Environ. Sci. Technol.* **2024**, *58*, 12823-45. DOI
20. Miller, D. M.; Liu, M. J.; Abels, K.; Kogler, A.; Williams, K. S.; Tarpeh, W. A. Engineering a molecular electrocatalytic system for energy-efficient ammonia production from wastewater nitrate. *Energy. Environ. Sci.* **2024**, *17*, 5691-705. DOI
21. Hao, R.; Song, Y.; Yang, L.; et al. Electrochemical reduction of flue gas denitrification wastewater to ammonia using a dual-defective Cu_2O@Cu heterojunction electrode. *Environ. Sci. Technol.* **2024**, *58*, 5557-66. DOI
22. Chen, X.; Cheng, Y.; Zhang, B.; Zhou, J.; He, S. Gradient-concentration RuCo electrocatalyst for efficient and stable electroreduction of nitrate into ammonia. *Nat. Commun.* **2024**, *15*, 6278. DOI PubMed PMC
23. Zhou, C.; Zhang, Y.; Xie, C.; et al. Efficient electroreduction of low nitrate concentration via nitrate self-enrichment and active hydrogen inducement on the Ce(IV)-Co_3O_4 cathode. *Environ. Sci. Technol.* **2024**, *58*, 14940-8. DOI

24. Chen, F. Y.; Wu, Z. Y.; Gupta, S.; et al. Efficient conversion of low-concentration nitrate sources into ammonia on a Ru-dispersed Cu nanowire electrocatalyst. *Nat. Nanotechnol.* **2022**, *17*, 759-67. DOI
25. Song, Z.; Liu, Y.; Zhong, Y.; Guo, Q.; Zeng, J.; Geng, Z. Efficient electroreduction of nitrate into ammonia at ultralow concentrations via an enrichment effect. *Adv. Mater.* **2022**, *34*, e2204306. DOI
26. Kazi, O. A.; Chen, W.; Eatman, J. G.; et al. Material design strategies for recovery of critical resources from water. *Adv. Mater.* **2023**, *35*, e2300913. DOI
27. Chen, S.; Wang, X.; Zheng, H.; et al. Electron-buffering rechargeable microelectrode adsorbents for rapid environmental remediation of uranium-containing wastewater. *Nat. Water.* **2025**, *3*, 937-48. DOI
28. Zhang, G.; Wang, F.; Chen, K.; Kang, J.; Chu, K. Atomically dispersed Sn confined in FeS_2 for nitrate-to-ammonia electroreduction. *Adv. Funct. Mater.* **2024**, *34*, 2305372. DOI
29. Zhou, B.; Tong, Y.; Yao, Y.; et al. Reversed I_1Cu_4 single-atom sites for superior neutral ammonia electrosynthesis with nitrate. *Proc. Natl. Acad. Sci. U. S. A.* **2024**, *121*, e2405236121. DOI PubMed PMC
30. Liu, M.; Yang, T.; Pan, Z.; et al. Bridging Li-ion batteries and fuel cells: from cathode leaching residue to an atomic-scale catalytic system. *ACS. Energy. Lett.* **2023**, *8*, 1652-61. DOI
31. Wang, C.; Kong, X.; Wang, L.; et al. Mechanistically engineered heterojunction from spent LFP for efficient oxygen evolution electrocatalysis. *Angew. Chem. Int. Ed. Engl.* **2025**, *64*, e202516122. DOI
32. Song, J.; Qian, S.; Yang, W.; et al. Nano-single-atom heterointerface engineering for pH-universal electrochemical nitrate reduction to ammonia. *Adv. Funct. Materials.* **2024**, *34*, 2409089. DOI
33. Su, J.; Shi, K.; Liu, B.; et al. Engineering the metal-support interaction and oxygen vacancies on Ru@P-Fe/Fe_3O_4 nanorods for synergetic enhanced electrocatalytic nitrate-to-ammonia conversion. *Adv. Funct. Mater.* **2024**, *34*, 2401194. DOI
34. Quan, F.; Zhan, G.; Xu, P.; et al. Electrochemical removal of nitrate in high-salt wastewater with low-cost iron electrode modified by phosphate. *J. Environ. Sci. (China).* **2025**, *148*, 38-45. DOI
35. Wen, W.; Yan, P.; Sun, W.; Zhou, Y.; Yu, X. Metastable phase Cu with optimized local electronic state for efficient electrocatalytic production of ammonia from nitrate. *Adv. Funct. Materials.* **2023**, *33*, 2212236. DOI
36. Xu, J.; Zhang, S.; Liu, H.; et al. Breaking local charge symmetry of iron single atoms for efficient electrocatalytic nitrate reduction to ammonia. *Angew. Chem. Int. Ed. Engl.* **2023**, *62*, e202308044. DOI
37. He, W.; Zhang, J.; Dieckhöfer, S.; et al. Splicing the active phases of copper/cobalt-based catalysts achieves high-rate tandem electroreduction of nitrate to ammonia. *Nat. Commun.* **2022**, *13*, 1129. DOI PubMed PMC
38. Zhang, Z.; Feng, X.; Zhang, Z.; et al. Graphdiyne enabled nitrogen vacancy formation in copper nitride for efficient ammonia synthesis. *J. Am. Chem. Soc.* **2024**, *146*, 14898-904. DOI
39. Liu, Y.; Zhuang, Z.; Liu, Y.; et al. Shear-strained Pd single-atom electrocatalysts for nitrate reduction to ammonia. *Angew. Chem. Int. Ed. Engl.* **2024**, *63*, e202411396. DOI
40. Zhang, S.; Wu, J.; Zheng, M.; et al. Fe/Cu diatomic catalysts for electrochemical nitrate reduction to ammonia. *Nat. Commun.* **2023**, *14*, 3634. DOI PubMed PMC
41. Li, J.; Li, M.; An, N.; et al. Boosted ammonium production by single cobalt atom catalysts with high Faradic efficiencies. *Proc. Natl. Acad. Sci. U. S. A.* **2022**, *119*, e2123450119. DOI PubMed PMC
42. Gu, Z.; Zhang, Y.; Wei, X.; Duan, Z.; Gong, Q.; Luo, K. Intermediates regulation via electron-deficient Cu sites for selective nitrate-to-ammonia electroreduction. *Adv. Mater.* **2023**, *35*, e2303107. DOI
43. Ye, S.; Chen, Z.; Zhang, G.; et al. Elucidating the activity, mechanism and application of selective electrosynthesis of ammonia from nitrate on cobalt phosphide. *Energy. Environ. Sci.* **2022**, *15*, 760-70. DOI
44. Li, P.; Jin, Z.; Fang, Z.; Yu, G. A single-site iron catalyst with preoccupied active centers that achieves selective ammonia electrosynthesis from nitrate. *Energy. Environ. Sci.* **2021**, *14*, 3522-31. DOI
45. Eziz, A.; Abulizi, A.; Liang, C.; et al. Doping-engineered Fe-Co tandem sites balance hydrogen and nitrite intermediates for efficient nitrate to ammonia conversion at low potential. *Small* **2026**, *22*, e73610. DOI
46. Zhang, J.; Liu, Y.; Zhang, J.; Guan, J.; Ke, H.; Huang, Y. Engineering single-atomic Ru sites on cobalt hydroxide boosts atomic hydrogen generation for efficient nitrate electroreduction to ammonia. *Renewables* **2025**, *3*, 99-110. DOI
47. Huang, P.; Fan, T.; Ma, X.; et al. 3D flower-like zinc cobaltite for electrocatalytic reduction of nitrate to ammonia under ambient conditions. *ChemSusChem* **2022**, *15*, e202102049. DOI
48. Wu, Z. Y.; Karamad, M.; Yong, X.; et al. Electrochemical ammonia synthesis via nitrate reduction on Fe single atom catalyst. *Nat. Commun.* **2021**, *12*, 2870. DOI PubMed PMC
49. Dong, K.; Han, S.; Li, Y.; et al. Testing, quantification, in situ characterization and calculation simulation for electrocatalytic nitrate reduction. *Nat. Protoc.* **2026**, *21*, 2707-62. DOI

50. Wang, H.; Huang, J.; Cai, J.; et al. *In situ*/*operando* methods for understanding electrocatalytic nitrate reduction reaction. *Small. Methods.* **2023**, *7*, e2300169. DOI

51. Souza, M. K. R.; Cardoso, E. S. F.; Pinto, L. M. C.; et al. Effective nitrate electroconversion to ammonia using an entangled Co_3O_4/graphene nanoribbon catalyst. *ACS. Appl. Mater. Interfaces.* **2025**, *17*, 1295-310. DOI

52. Liu, Y.; Wei, J.; Yang, Z.; et al. Efficient tandem electroreduction of nitrate into ammonia through coupling Cu single atoms with adjacent Co_3O_4. *Nat. Commun.* **2024**, *15*, 3619. DOI PubMed PMC